

Physically constrained 2D joint inversion of surface and body wave tomography

Original

Physically constrained 2D joint inversion of surface and body wave tomography / Karimpour, Mohammadkarim; Slob, Evert Cornelis; Socco, Laura Valentina. - In: JOURNAL OF ENVIRONMENTAL & ENGINEERING GEOPHYSICS. - ISSN 1083-1363. - ELETTRONICO. - 27:2(2022), pp. 57-71. [10.32389/JEEG21-031]

Availability:

This version is available at: 11583/2968546 since: 2022-06-22T18:52:22Z

Publisher:

Environmental and Engineering Geophysical Society (EEGS)

Published

DOI:10.32389/JEEG21-031

Terms of use:

This article is made available under terms and conditions as specified in the corresponding bibliographic description in the repository

Publisher copyright

(Article begins on next page)

Physically Constrained 2D Joint Inversion of Surface and Body Wave Tomography

Mohammadkarim Karimpour^{1,*}, Evert Cornelis Slob² and Laura Valentina Socco¹

¹Politecnico di Torino, Torino 10129, Italy

²Delft University of Technology, Delft 2628 CN, Netherlands

*Corresponding author email: mohammadkarim.karimpour@polito.it

ABSTRACT

Joint inversion of different geophysical methods is a powerful tool to overcome the limitations of individual inversions. Body wave tomography is used to obtain P-wave velocity models by inversion of P-wave travel times. Surface wave tomography is used to obtain S-wave velocity models through inversion of the dispersion curves data. Both methods have inherent limitations. We focus on the joint body and surface waves tomography inversion to reduce the limitations of each individual inversion. In our joint inversion scheme, the Poisson ratio was used as the link between P-wave and S-wave velocities, and the same geometry was imposed on the final velocity models. The joint inversion algorithm was applied to a 2D synthetic dataset and then to two 2D field datasets. We compare the obtained velocity models from individual inversions and the joint inversion. We show that the proposed joint inversion method not only produces superior velocity models but also generates physically more meaningful and accurate Poisson ratio models.

INTRODUCTION

Surface wave methods are usually used to retrieve S-wave velocity models, and body wave tomography (BWT) based on travel times inversion is used to obtain P-wave velocity distribution. Regardless of the chosen approach, inversion is an important step to obtaining subsurface velocity models, and non-uniqueness is an inherent problem of all geophysical inversion methods (Menke, 1989). Surface wave inversion is ill-posed and strongly nonlinear. In BWT, some subsurface layers may not be recovered properly. This can be due to the presence of strong velocity contrasts, velocity inversions, or thin layers (Reynolds, 1997).

Joint inversion approaches aim to reduce the problems associated with geophysical data inversion. In joint inversion methods, different types of geophysical data that contain complementary information are inverted together to yield a more consistent final model, which is representative of all the data.

Joint inversion approaches can be classified into two main groups: structural and petrophysical joint inversion (Garofalo, 2014). Structural-based methods impose the same geometry on the model. On the other hand, in petrophysical joint inversion approaches, not only the subsurface structure is considered the same, but also model parameters are related to each other through petrophysical relationships.

There are different approaches for structural coupling in joint inversion. Gallardo and Meju (2003)

introduced cross-gradient as a structural constraint in the joint inversion of direct-current resistivity and seismic travel time data. Hu *et al.* (2009) employed cross-gradient as the structural link between P-wave velocity and electromagnetic data. Ogunbo *et al.* (2018) applied joint inversion on seismic travel times and the frequency domain electromagnetic data using cross-gradient as the structural link. Paulatto *et al.* (2019) used joint inversion of first arrival travel times and gravity data with cross-gradient constraints to model a magmatic system. Haber and Gazit (2013) suggested another approach called joint total variation, in which the structural similarity was measured based on the norms of the absolute spatial gradient values of the models. Lien (2013) proposed a method for the structural coupling of model parameters in which the structure was considered as a transition between dominating parameter values and inverted for a common model parameter that represented the structure in the different parameter fields.

Using petrophysical relationships, when available, can further improve the joint inversion results. Ghose and Slob (2006) showed improvements in non-uniqueness problems exploiting petrophysical relationships in a joint inversion of ground-penetrating radar and seismic reflection data. Gao *et al.* (2010) used porosity as the physical link in the joint inversion of seismic and EM data. They employed a petrophysical relationship (Gassmann equation) to get the porosity from P-wave velocities and then applied Archie's law to transform the computed porosities

into resistivity values. Dell'Aversana *et al.* (2011) applied empirical petrophysical relationships in their joint inversion scheme to reduce the ambiguity of well-log data interpretation. Moorkamp *et al.* (2011) calculated conductivities and densities from P-wave velocities using empirical relationships. Carter-McAuslan *et al.* (2015) demonstrated how fuzzy c-means clustering could be used for coupling physical properties in joint inversion. Wagner *et al.* (2019) estimated the volumetric fractions of water, ice, air, and the rock matrix from petrophysical joint inversion of seismic refraction and electrical resistivity data.

Several researchers have applied different joint inversion schemes in near-surface studies. Comina *et al.* (2002) suggested a 1D joint inversion of surface wave data and apparent resistivity based on the layered model parameterization. Piatti *et al.* (2013) proposed a 1D joint inversion scheme for surface wave data and P-wave travel times. They demonstrated that some low S-wave and P-wave velocity layers which could not be detected by individual inversions could be modeled using joint inversion. Garofalo *et al.* (2015) suggested an algorithm for the joint inversion among surface wave data, P-wave travel times, and apparent resistivity data. They applied the structural coupling among the methods, as well as the Poisson ratio as the physical link between S-wave and P-wave velocities.

The current paper focuses on the joint inversion of surface wave tomography (SWT) and BWT with the Poisson ratio as the physical link, using a layered model parameterization strategy. The previous study has demonstrated that BWT and 1D surface wave analysis (SWA) can be merged in a joint inversion scheme (Boiero and Socco, 2014). Here SWT replaces SWA. In SWA, each dispersion curve (phase velocity as a function of frequency) is assigned to one position along the acquisition line, and since the final model is a collection of 1D local models, it might be laterally smoothed. However, in SWT, each dispersion curve (DC) is estimated between a receiver pair, and the forward operator considers the lateral variability in the computation of the path-averaged slowness between the receiver pair. Due to its ability to produce high-resolution 2D or 3D S-wave velocity models, SWT has recently gained considerable attention in near-surface applications (Krohn and Routh, 2017; Papadopoulou *et al.*, 2020; Da Col *et al.*, 2020, Khosro Anjom, 2021). However, SWT inversion still suffers from ill-posedness and non-uniqueness. This issue can be addressed using the joint inversion of SWT and BWT.

In the remaining part of the paper, first, we describe the applied algorithm, then we apply the joint inversion scheme on 2D synthetic and field datasets and compare the results with individual inversions.

METHOD

The input data for the joint inversion of SWT and BWT are dispersion curves and P-wave travel times $\mathbf{tt}(xr, xs)$, respectively. Travel times are functions of receiver position xr and source position xs . Here, the travel times are manually picked on the seismograms. If the S/N ratio of the recorded signal is poor at a receiver location, which may happen particularly at far offset due to attenuation, the travel time is not picked for the corresponding trace. Dispersion curves are computed using a modified two-station method (see Da Col *et al.*, 2020 for details). For a 2D line with nr being the number of receivers, the total number of unique receiver pairs are $\frac{(nr-1)*nr}{2}$. Each dispersion curve $\mathbf{dc}(xr, f)$ is extracted between a pair of receivers aligned with a source. The lateral variations can be characterized by using this data redundancy (Boiero and Socco, 2010).

The input data are integrated into the observed data vector \mathbf{d}_{obs} as:

$$\mathbf{d}_{obs} = [\mathbf{dc}(xr, f), \mathbf{tt}(xr, xs)]^T. \quad (1)$$

The data uncertainty is described by the covariance matrix \mathbf{C}_{obs} as:

$$\mathbf{C}_{obs} = \begin{bmatrix} \mathbf{C}_{dc} & 0 \\ 0 & \mathbf{C}_{tt} \end{bmatrix}, \quad (2)$$

where \mathbf{C}_{dc} represents the covariance matrix of DC data, \mathbf{C}_{tt} is the covariance matrix for travel times. As it is often assumed, the data covariance matrix, \mathbf{C}_{obs} , is diagonal in our case. However, \mathbf{C}_{obs} may no longer be diagonal if the modeling error is considered in the computation of the data uncertainty (see Bai *et al.*, 2021, for details).

The subsurface model is parameterized into a 2D set of cells. In our 2D parameterization, the width of cells and the number of layers nl should be defined. The width of the cells does not change during the inversion process. The height of each cell is a model parameter and corresponds to the layer thickness h . Besides the layer thickness, the model parameters at each cell are S-wave velocity VS , P-wave velocity VP , and density ρ . We assume that the density values are known a priori information. The vector of unknown model parameters for the cell corresponding to the i^{th} layer and the j^{th} cell along the horizontal axis is defined as:

$$\mathbf{m}_{i,j}(h_{i,j}, VS_{i,j}, VP_{i,j}) = [h_{i,j}; VS_{i,j}; VP_{i,j}]. \quad (3)$$

The unknown model parameters for the 2D media are expressed by the matrix \mathbf{m}_{2D} :

$$\mathbf{m}_{2D} = \begin{bmatrix} \mathbf{m}_{1,1}(h_{1,1}, VS_{1,1}, VP_{1,1}) & \dots & \mathbf{m}_{1,k}(h_{1,k}, VS_{1,k}, VP_{1,k}) \\ \vdots & & \vdots \\ \mathbf{m}_{nl,1}(h_{nl,1}, VS_{nl,1}, VP_{nl,1}) & \dots & \mathbf{m}_{nl,k}(h_{nl,k}, VS_{nl,k}, VP_{nl,k}) \end{bmatrix}, \quad (4)$$

where k is the number of defined cells along the horizontal axis. The model parameters of the 2D model \mathbf{m}_{2D} are re-organized into the model vector \mathbf{m} as:

$$\mathbf{m} = [\mathbf{m}_{1,1}(b_{1,1}, VS_{1,1}, VP_{1,1}); \dots; \mathbf{m}_{nl,k}(b_{nl,k}, VS_{nl,k}, VP_{nl,k})]. \quad (5)$$

The forward response $fw(\mathbf{m})$ of the model \mathbf{m} is given by:

$$fw(\mathbf{m}) = \begin{bmatrix} fw_{SWT}(\mathbf{m}) \\ fw_{BWT}(\mathbf{m}) \end{bmatrix}, \quad (6)$$

where $fw_{SWT}(\mathbf{m})$ and $fw_{BWT}(\mathbf{m})$ are the forward response for SWT and BWT, respectively. In the forward modeling of the surface wave tomography $fw_{SWT}(\mathbf{m})$, for each DC, the path between the corresponding receiver pair is discretized to many points (every 10 cm). For each frequency at each point, the slowness is obtained as the linear interpolation between the slowness of the two surrounding cells. Then, for each frequency, the path-averaged slowness is computed as the mean of the slowness of all the discretized points. So, in SWT forward modeling, differently from conventional local 1D surface wave analysis, the lateral variations along the path are also considered. The forward response of BWT $fw_{BWT}(\mathbf{m})$ is computed by a 2D finite difference method proposed by Noble *et al.* (2014).

The inverse problem is solved by minimizing the misfit function Φ , which is defined as:

$$\Phi = \left[(\mathbf{d}_{obs} - fw(\mathbf{m}))^T \mathbf{C}_{obs}^{-1} (\mathbf{d}_{obs} - fw(\mathbf{m})) \right] + \left[(-\mathbf{Rm})^T \mathbf{C}_R^{-1} (-\mathbf{Rm}) \right] \quad (7)$$

the variation of each model parameter between the neighboring cells is controlled by the spatial regularization matrix \mathbf{R} , which has values of +1 and -1 for the linked model parameters and zeros elsewhere. The strength of this link is determined by the covariance matrix of spatial regularization \mathbf{C}_R (see Auken and Christiansen, 2004, for details). The values of \mathbf{C}_R are chosen based on the available a priori information. Stronger constraints lead to a smoother final model. For weak, medium, and strong constraints, the values of \mathbf{C}_R can be set to 10^4 , 1, and 0.01, respectively, and a value of 10^6 can be used to remove the impact of the spatial regularization (Boiero and Socco, 2010).

The model is updated at each iteration, aiming to minimize the misfit function in Eq. 7. A quasi-Newton damped least-squares algorithm (Tarantola, 1987) is employed for the misfit minimization. At the n^{th} iteration, the model \mathbf{m}_n is updated to \mathbf{m}_{n+1} as:

$$\mathbf{m}_{n+1} = \mathbf{m}_n + \left(\begin{bmatrix} \mathbf{G}_J^T \mathbf{C}_{obs}^{-1} \mathbf{G}_J + \mathbf{R}^T \mathbf{C}_R^{-1} \mathbf{R} + \lambda \mathbf{I} \end{bmatrix}^{-1} \times \begin{bmatrix} \mathbf{G}_J^T \mathbf{C}_{obs}^{-1} (\mathbf{d}_{obs} - fw(\mathbf{m}_n)) + \mathbf{R}^T \mathbf{C}_R^{-1} (-\mathbf{Rm}_n) \end{bmatrix} \right) \quad (8)$$

where λ stands for the damping factor which stabilizes the solution (for details, see Marquardt, 1963), and \mathbf{G}_J represents the sensitivity matrix of the data, which is given by:

$$\mathbf{G}_J = \begin{bmatrix} \mathbf{G}_{J,SWT} \\ \mathbf{G}_{J,BWT} \end{bmatrix} \quad (9)$$

where $\mathbf{G}_{J,SWT}$ and $\mathbf{G}_{J,BWT}$ are the sensitivity matrix of SWT and BWT, respectively.

Since the elements of \mathbf{m}_n have different physical dimensions and sensitivities can be different by orders of magnitudes, normalization is important for the stability of the results. Therefore, following the normalization approach proposed by Boiero and Socco (2014), all elements of \mathbf{m}_n , and all quantities related to \mathbf{m}_n , such as \mathbf{G}_J , are normalized with respect to \mathbf{m}_n . Also, the \mathbf{d}_{obs} and the terms related to it like $fw(\mathbf{m}_n)$ and \mathbf{C}_{obs} are normalized to \mathbf{d}_{obs} . At each iteration of the joint inversion, it is possible that the computed values of the Poisson ratio are not physical (in the range of 0–0.5). If this problem occurs, the damping factor is changed until at least 75% of all Poisson ratio values in the computed model \mathbf{m}_{n+1} have physical values. Then, for each cell with a non-physical Poisson ratio value, new P-wave and S-wave velocities are computed by averaging the corresponding values of the closest cells which have physical Poisson ratio values. Having computed new velocities for these grids, new Poisson ratio values are computed. Having a physical Poisson ratio for all cells, the inversion process continues to the next iteration. The iterative process stops when either the number of iterations exceeds 40 or the misfit value of the updated model (\mathbf{m}_{n+1}) decreases less than 0.01% of the misfit value of the previous model (\mathbf{m}_n).

Since all the following examples contain sharp lateral variations, we set the values of the spatial covariance matrix \mathbf{C}_R to 10^6 to damp the impact of the spatial regularization. It should be noted that there are different methods for spatial regularization. For instance, some approaches promote the sparse reconstruction of the model (see Vignoli *et al.*, 2021 for details). In this work, we focus on the physical constraint in the joint inversion of SWT and BWT, which acts as a smoothing operator for the inversion cells with non-physical values of the Poisson ratio.

Table 1 Geophysical parameters of the model (Karimpour *et al.*, 2021).

Layer	VS (m/s)	VP (m/s)	h (m)	ρ (g/cm ³)
1	180	310	2	2
2	320	590	3–8	2.1
Half-space	480	950	–	2.2

Table 2 Geophysical parameters of the initial model (Karimpour *et al.*, 2021).

Layer	VS (m/s)	VP (m/s)	h (m)	ρ (g/cm ³)
1	200	300	3	2
2	300	600	6	2.1
Half-space	500	930	–	2.2

RESULTS AND DISCUSSIONS

Synthetic Example

The synthetic data have been generated using a finite difference code (see Qin *et al.*, 2020 for details). The model presents a vertical uplift in the bottom-right part of the model. The source emits a 20 Hz Ricker wavelet. The receivers are located every meter along the line, and there are 25 shots with 5 m spacing. The seismic properties of the model are presented in Table 1. The P- and S-wave velocity values and the Poisson ratio distribution of the model are shown in Figs. 1(a)–(c), respectively.

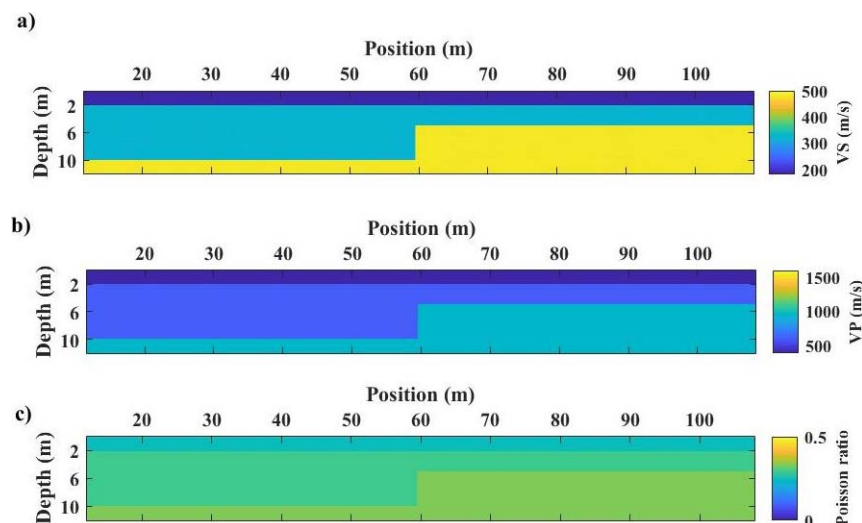
The dispersion curves were retrieved by applying a modified two-station method (Da Col *et al.*, 2020) to different receiver couples. To select the receiver pairs, the considered minimum distance between receivers was 4 m, and the maximum distance was equal to 34 m. For each selected receiver couple, the obtained cross-correlation matrices from different shots were stacked to increase the signal-to-noise ratio. The travel times were picked manually on the seismograms. A 1% uncertainty was associated with all travel times data, and the uncertainty values of the DC data are computed based on the equation proposed by Passeri (2019):

$$\sigma_V = [0.2822e^{-0.1819f} + 0.0226e^{0.0077f}] * V \quad (10)$$

where V represents the phase velocity, σ_V is the standard deviation of the phase velocity, and f is the frequency. The estimated DCs and the picked first-arrival times are depicted in Figs. 2(a) and 2(b), respectively.

Initial model. A laterally homogeneous model was defined as the initial model. The initial model consisted of 3 layers, including the half-space. The thickness of the first two layers was assumed to be 3 m. The initial seismic velocities were chosen close to the true values. The seismic properties of the initial model that was used in the inversion scheme are presented in Table 2. The average relative error between the initial VP and VS models and the true model is 14.22 % and 16.55 %, respectively.

Inversion results. The considered width of the inversion cells was 6 m. The initial model was updated based on Eq. 8 until it satisfied the stopping criteria. Very weak constraints were set for a priori information so that mostly the experimental data contribute to the solution. Hence, the value of the elements of C_R were set equal to 10^6 . The same initial model was used to perform individual inversions and joint inversions. Figure 3 shows the normalized (per data number) misfit Φ values at each iteration for individual and joint inversions. Assuming the data are not redundant, the larger the dataset, the harder it becomes to reduce the misfit. Even though the joint inversion scheme deals with a larger dataset, it generated a lower final misfit

**Figure 1** (a) VS distribution of the true model, (b) VP distribution of the true model, and (c) Poisson ratio of the true model.

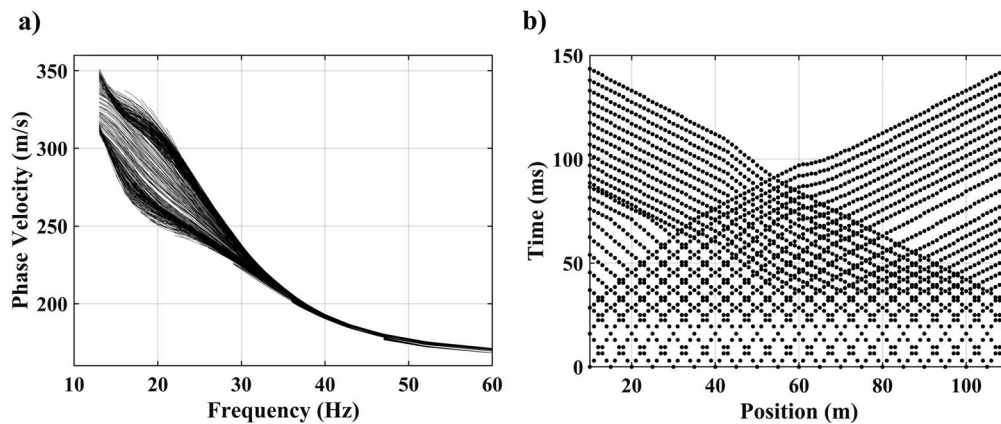


Figure 2 The input data for the inversion process: (a) all extracted dispersion curves and (b) picked P-wave travel times.

than both individual inversions. This suggests that there is indeed more information in combining the two datasets than in either single dataset. The joint inversion also stopped a few iterations before individual BWT (14 against 18 iterations).

The generated velocity models by joint inversion and individual inversions are displayed in Figs. 4 and 5. As shown in Fig. 4, the second interface is much better recovered in the joint inversion compared to the individual SWT. In the case of individual BWT inversion (Fig. 5(a)), the variation of the VP values in the third layer is considerably high, with a maximum velocity of more than 1,600 m/s, which is far from the true value (950 m/s). This variation is reduced significantly by applying the joint inversion algorithm (Fig. 4(b)). The velocity models in Figs. 4 and 5 are used to compute an average error relative to the true velocity models. The obtained velocity models from the joint inversion algorithm have lower average errors with respect to individual inversion

results. In the case of VS models (Fig. 4), the joint inversion produces a model with an average error equal to 8.62%, while this error for the VS model from individual SWT is 12.51%. For VP models (Fig. 5), the average errors for the models from joint inversion and individual BWT are 8.49% and 9.06%, respectively. The obtained velocity models from individual SWT and BWT inversions are used to compute a Poisson ratio distribution (Fig. 6(a)). This Poisson ratio model contains non-physical values in many locations. However, the generated Poisson ratio model from the joint inversion (Fig. 6(b)) is both physically meaningful and close to the true model. Even though the initial model has Poisson ratio values that are far from the true values (average error of 22.4%), the obtained Poisson ratio from the joint inversion algorithm is, with an average error of 5.2%, substantially more accurate than the individual inversions.

Field Example 1: CNR

Site description and field data. The field data were acquired at the National Research Council (CNR) headquarter in Turin, Italy. The site consists of compacted sand and gravel formation surrounding an artificial loose sand body. The extent of the sand body is an area of 5 m × 5 m at the surface, with the maximum depth equal to 2.5 m.

The data were acquired along a 2D line crossing the sand body. The acquisition was carried out using an 8 kg hammer source in 11 positions. The data were recorded using 72 vertical 4.5 Hz geophones with 0.3 m spacing. A detailed description of the dataset can be found in Teodor *et al.* (2017). The acquisition outline is depicted in Fig. 7.

Dispersion curves were estimated using the modified two-station method (for details, see Da Col *et al.*, 2020). The chosen minimum and maximum distances for the selection of receiver pairs were equal

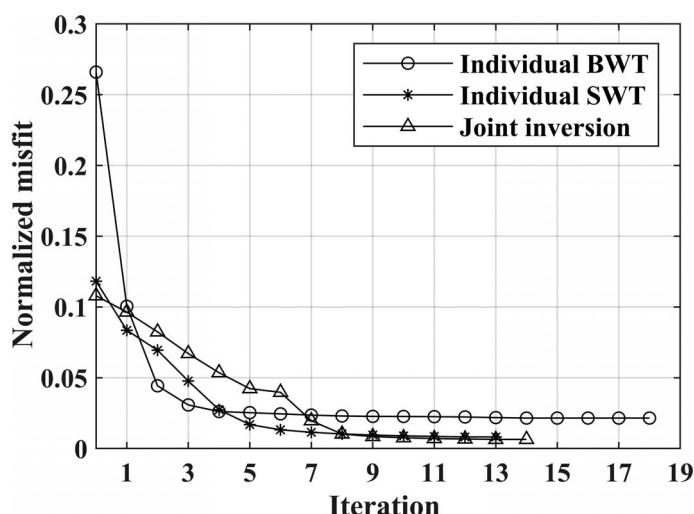


Figure 3 Comparison of the normalized misfit value at each iteration for different inversions.

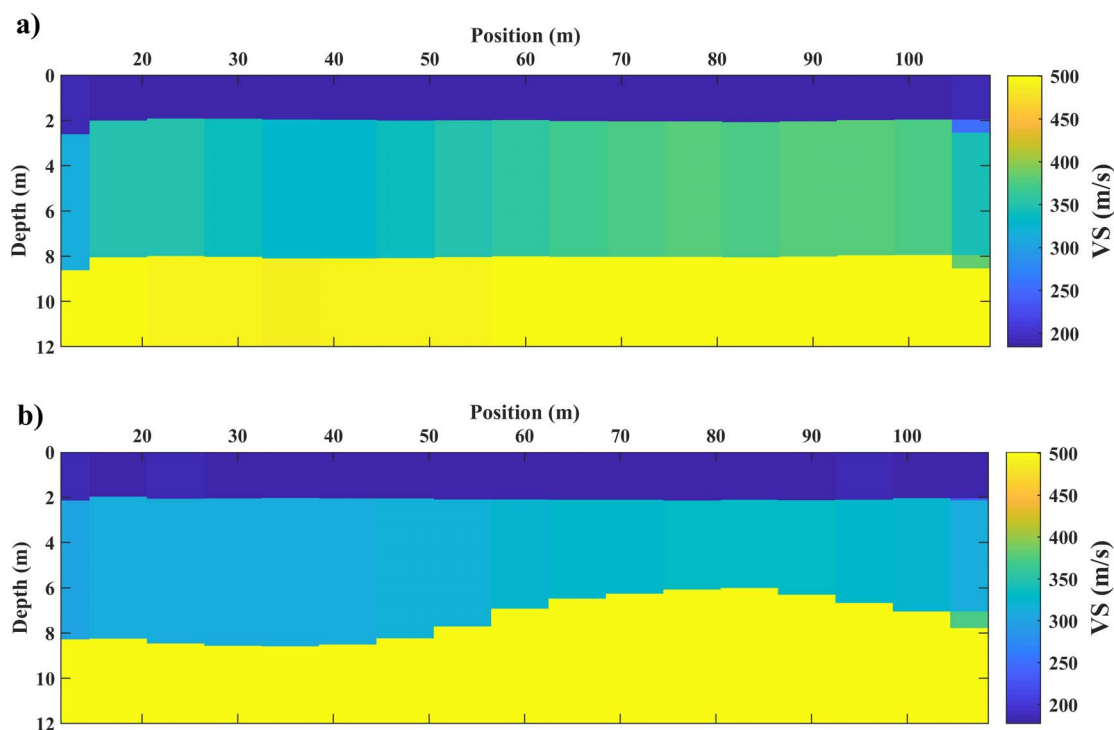


Figure 4 VS models from (a) individual SWT inversion and (b) BWT and SWT joint inversion.

to 2.1 m and 9.9 m, respectively. All the extracted DCs and the picked travel times are shown in Fig. 8. The frequency band of the DCs varies from 11 Hz to 86 Hz, and the wavelength ranges from 0.68 m to 77 m. The assigned uncertainties of the travel times are 1%, and the experimental uncertainties of the DCs are computed using Eq. 10.

Model parameterization and the initial model. The defined initial model was laterally homogeneous. The assigned width of all cells was 1 m. The assigned number of layers was equal to 5 (including the half-space). The thickness of all layers was assumed to be 1 m. The values of the spatial covariance matrix C_R were set equal to 10^6 . To obtain

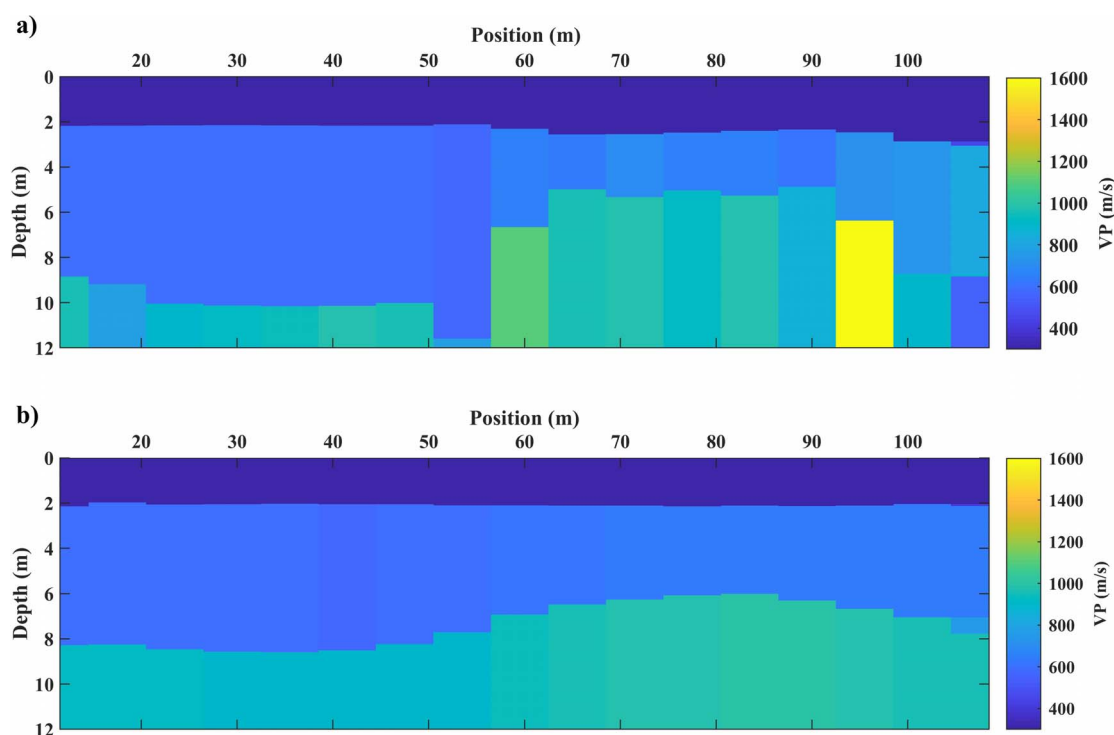


Figure 5 VP models from (a) individual BWT inversion and (b) BWT and SWT joint inversion.

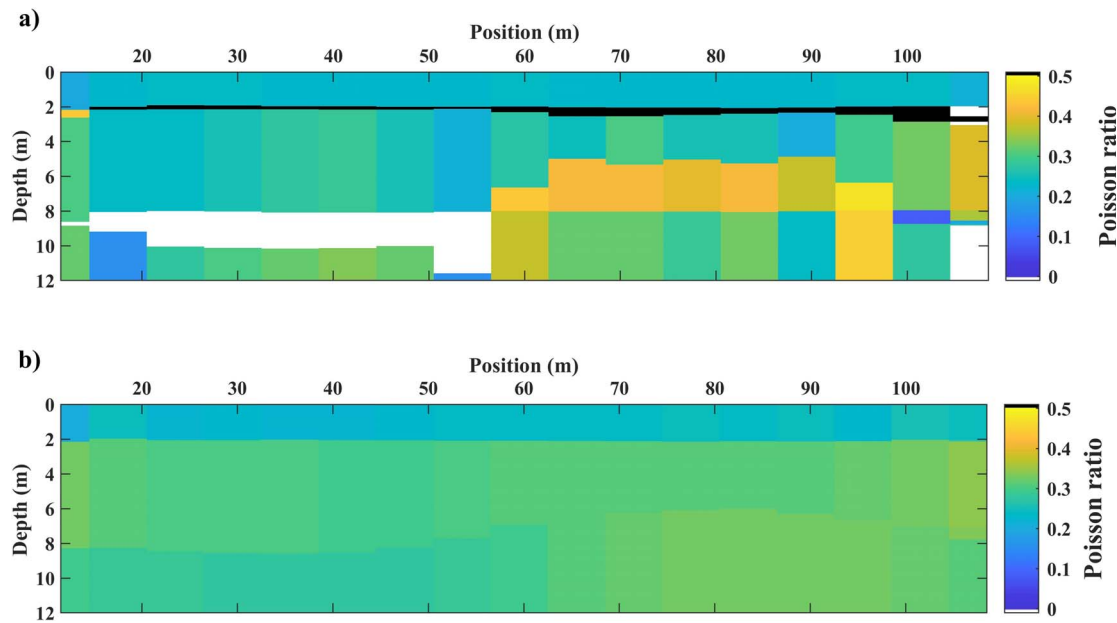


Figure 6 The obtained Poisson ratio model from (a) individual inversions and (b) BWT and SWT joint inversion.

the initial VS values, the DC with the broadest frequency band was plotted as a function of pseudo-depth (half-wavelength), and the phase velocities were averaged in the pseudo-depth range corresponding to each layer interval. The initial Poisson ratio values were set equal to 0.33 for all layers. The initial VP model was derived from the computed initial VS and Poisson ratio values. The initial model parameters are reported in Table 3.

For each estimated DC, the wavelength values were computed, and the wavelength coverage was obtained by computing the number of rays crossing each cell of the initial model (Fig. 9(a)). The ray path of travel times corresponding to the initial VP model is displayed in Fig. 9(b). Very weak constraints were set for a priori information so that mostly experimental data contribute to the solution.

Inversion results. Individual and joint inversions were carried out on the same initial model, a priori information, and constraint values. The normalized misfit values for different inversions, as a function

of iteration number, are displayed in Fig. 10, and the obtained velocity models are displayed in Figs. 11 and 12. Figure 10 shows that the joint inversion algorithm has both a lower misfit value and faster convergence than individual BWT inversion. The SWT inversion seems to get trapped in a local minimum, whereas the joint inversion gives a better VS model, even though with a slightly higher misfit value. This suggests a modification of the solution space and hence the benefit of extra information in the integration of the two datasets. Although the velocity contrast between the sandbox and the rest of the subsurface can be observed in the models from individual inversions, the joint inversion velocity models provide a much clearer image of this contrast. Moreover, the gradual increase of the velocities with depth inside the sand body is more obvious in the joint inversion results (Figs. 11(b) and 12(b)). Furthermore, the smooth lateral variation of the depth boundary of the sand deposit is well recovered by the joint inversion algorithm.

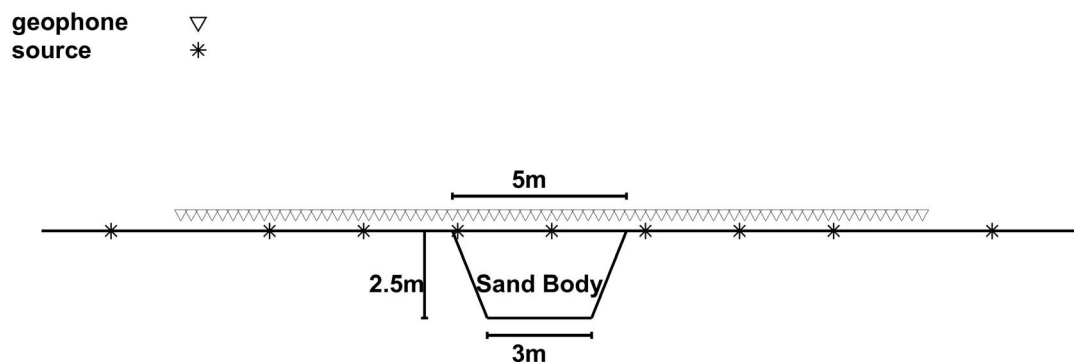


Figure 7 Acquisition outline of the field data.

Table 3 Initial model properties for the physical joint inversion.

Layer	h (m)	ρ (g/cm ³)	ν	VS (m/s)	VP (m/s)
1	1	2	0.33	100	200
2	1	2	0.33	120	240
3	1	2.1	0.33	150	300
4	1	2.1	0.33	190	380
Half-space	—	2.2	0.33	260	520

Figure 13 depicts the ray path of the travel times corresponding to the VP models in Fig. 12. As mentioned previously in the method section, during the joint inversion process, some cells may have non-

physical Poisson ratio values. This problem can be solved by averaging the velocities of adjacent cells or changing the damping factor. Figure 14 shows that only a couple of cells in the last iteration of the joint inversion have non-physical Poisson ratio values. Hence, new velocities for each of these cells were computed by averaging the velocities of the neighboring cells. The obtained Poisson ratio distribution from individual inversions and joint inversion is shown in Fig. 15. The computed Poisson ratio model from individual consists of non-physical values in several locations. However, the obtained Poisson ratio values

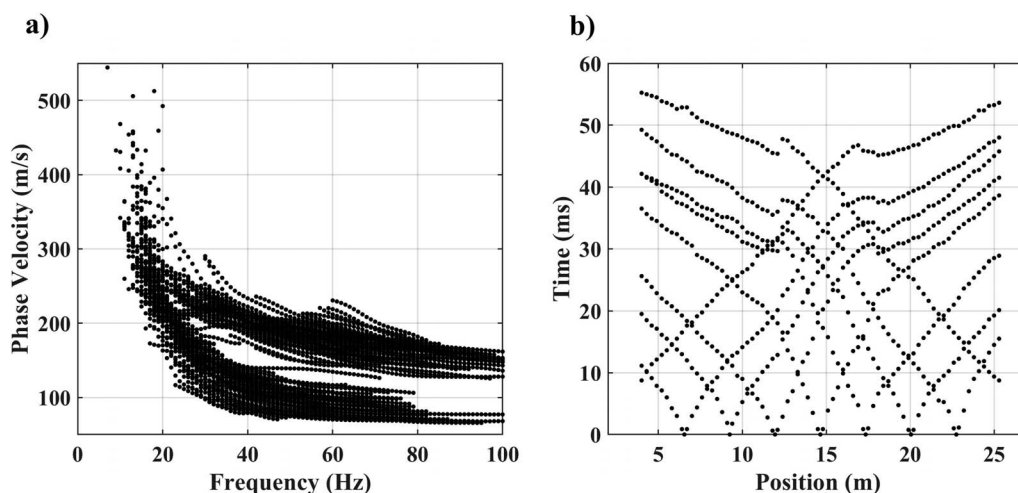


Figure 8 Input data for the inversion: (a) dispersion curves, (b) first arrival times.

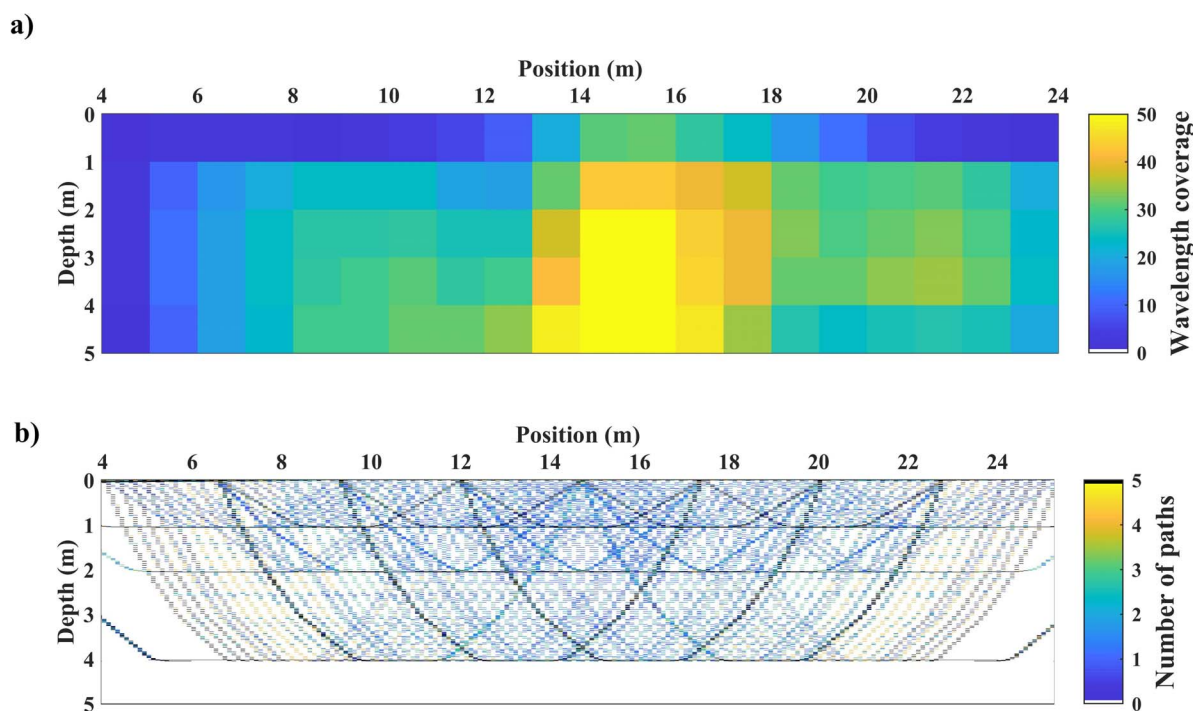


Figure 9 (a) The wavelength coverage of the retrieved DCs, (b) The ray path of the travel times corresponding to the initial VP model.

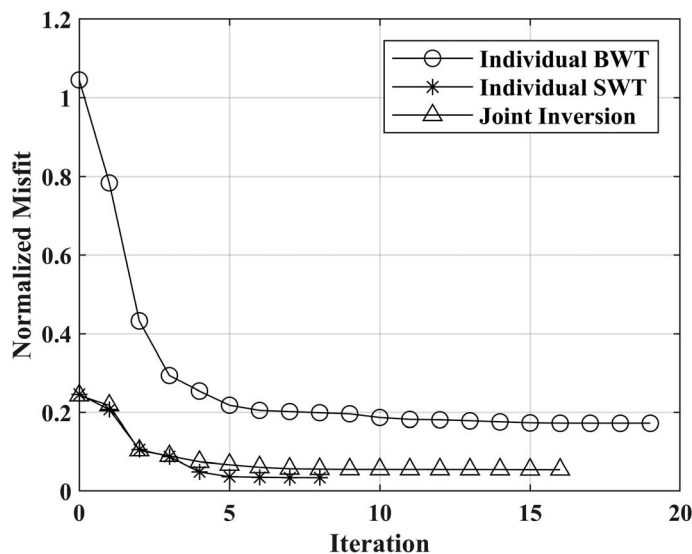


Figure 10 Comparison of the normalized misfit value at each iteration for different inversions.

from the joint inversion algorithm (Fig. 15(b)) do not suffer from this problem.

Field Example 2: Pijnacker

Site description and data acquisition. The data were acquired in a field close to Pijnacker, Netherlands. The available well data (Fig. 16) show that the field consists of clay, peat, and sand. The source was a vibrator that emitted a linear sweep signal from 2 to 100 Hz for 5 s at a force level of 1,150 N. The data were recorded by 120 vertical 4.5 Hz

geophones with 0.5 m spacing and 16 shot points with 5 m spacing (Fig. 16). The DCs were extracted from the raw data using an auto-picking code (Papadopoulos, 2021). Theoretically, a maximum number of 7140 pairs could be estimated from the 120 receivers. The code computes the DC for every possible receiver pair. Since the DC is an inherently smooth function between the phase velocity and frequency, if the smoothness of a DC shows ‘breaks’, it is rejected. Moreover, an automatic quality control (QC) approach is applied to the automatically picked DCs. A sub-set of the DCs is also picked manually, and the similarity of the automatically picked DCs to the manually picked DCs is evaluated. Then, the automatically picked DCs with low-quality are rejected (see Papadopoulos, 2021, for details). Due to the low quality of the data, a significant amount of the DCs were rejected, and only 175 DCs were obtained with a frequency band of 11–78 Hz and wavelengths between 0.7 m and 74.8 m. All the picked travel times and DCs are displayed in Fig. 17. The uncertainties of the DCs are computed using Eq. 10, and the travel times are assigned 1% uncertainties.

Model parameterization and the initial model. An 8-layer laterally homogeneous model was defined as the initial model. The cell width was equal to 1 m for all cells. The thickness was 1 m for the first four layers and 2 m for the deeper layers. The DC with the broadest frequency band was plotted as a function of pseudo-depth (half wavelength), and the mean value of the phase velocities in the pseudo-depth range corresponding to each layer interval was computed to obtain the initial VS model. The initial

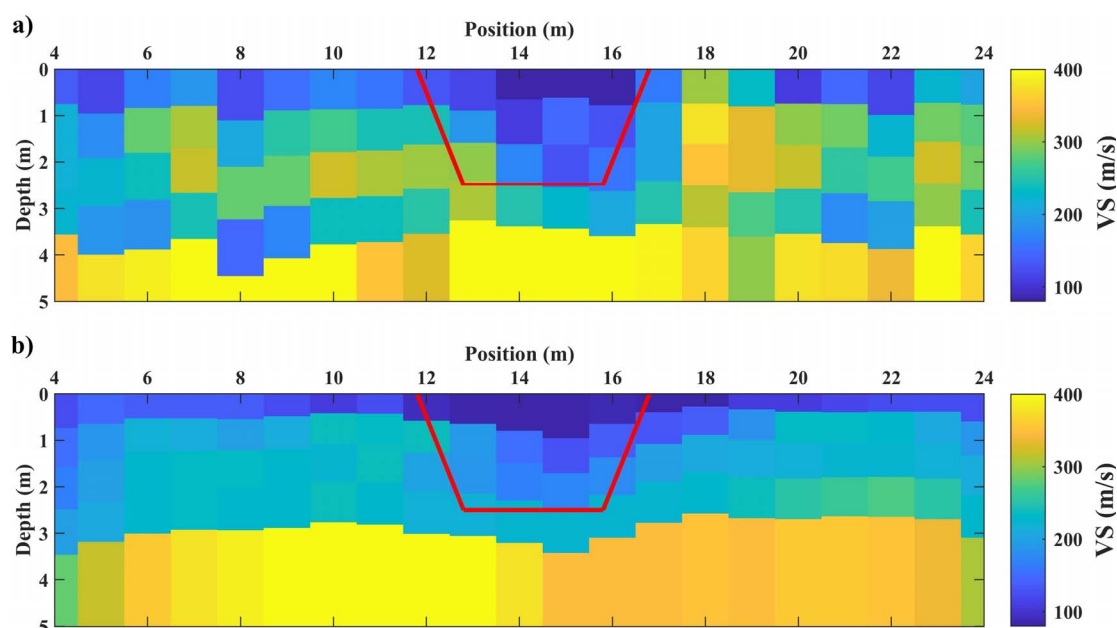


Figure 11 The obtained VS models are superimposed with the sand body shape in red from (a) individual SWT inversion and (b) BWT and SWT joint inversion.

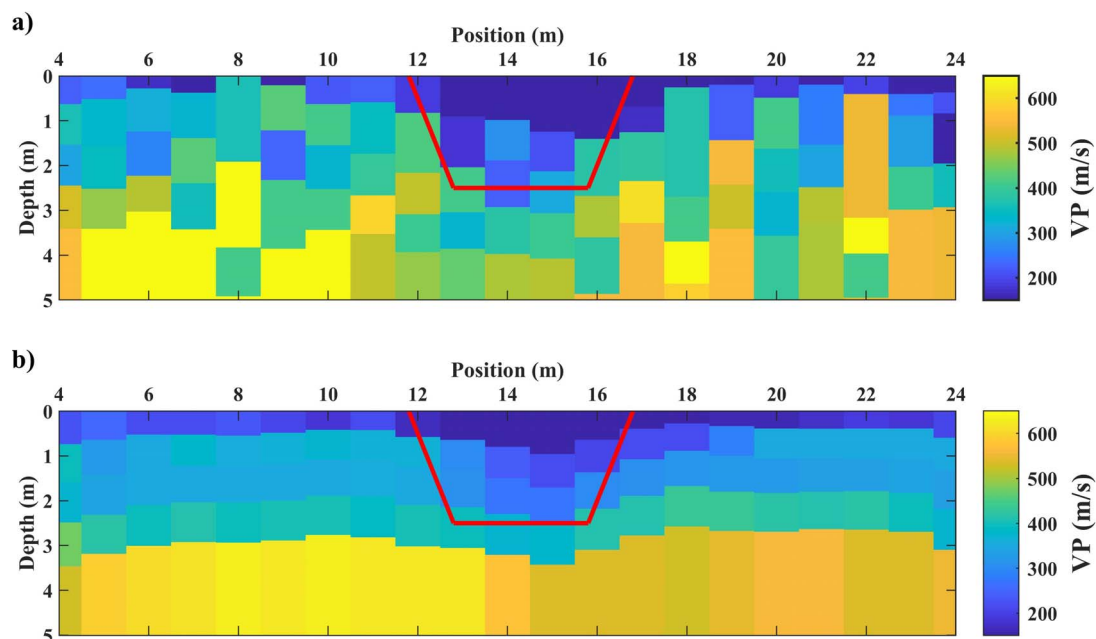


Figure 12 The obtained VP models with the sand body shape superimposed in red lines. VP models from (a) individual BWT inversion and (b) BWT and SWT joint inversion.

Poisson ratio values were defined as 0.3 for the first four layers and 0.4 for the deeper portions of the model. The initial VP values were computed from the obtained VS and Poisson ratio values. Also, in this case, the values of the covariance matrix C_R were set equal to 10^6 . Figure 18 shows the initial velocity models.

Inversion results. The same initial model and a priori information were used for joint and individual

inversions. Figure 19 displays the normalized misfit values as a function of iteration. It shows that the final misfit of joint inversion is slightly higher than individual SWT and that it has faster convergence and lower misfit than individual BWT. The obtained velocity models are depicted in Figs. 20 and 21.

A previous full-waveform inversion study was performed in a clay field near to Pijnacker in which

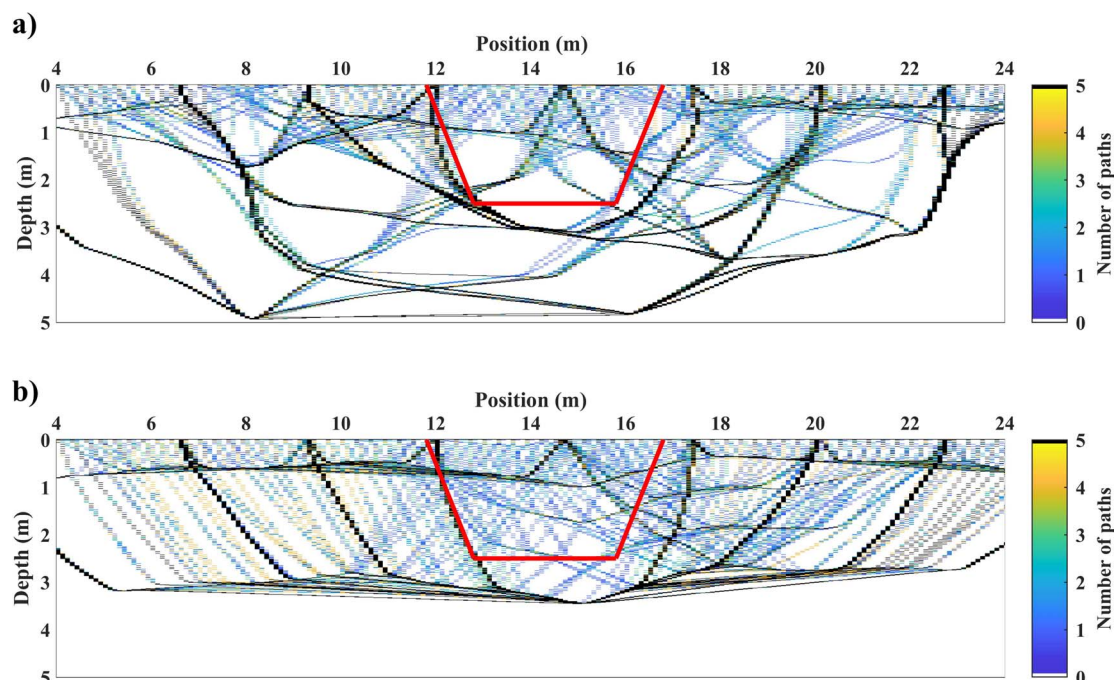


Figure 13 The ray path of first-arrival times from (a) individual BWT inversion and (b) BWT and SWT joint inversion. The sand body shape is shown in black lines.

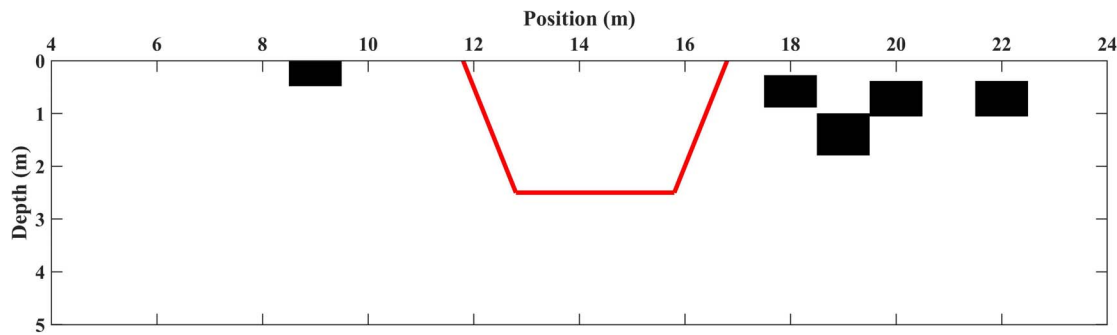


Figure 14 The cells with non-physical Poisson ratio values in the last iteration of BWT and SWT joint inversion are shown in black.

the estimated VS values were in the range of 40–80 m/s (Bharadwaj *et al.*, 2015). This range of VS value can be seen in the obtained VS models from both individual SWT and joint inversion (Figs. 20(a) and 20(b)), particularly in the shallower portions. This range of VS can be indicative of layers of clay and peat, and the levels with higher VS values (120–150 m/s) are associated with sand layers. In the most parts of the obtained VS model from individual SWT (Fig. 20(a)), higher VS values exist at the depth interval of 4–9 m, while in the VS model from joint inversion (Fig. 20(b)), the higher VS values mainly exist at levels either deeper than 10 m or depth interval of 4–6 m. In the obtained VP model from joint inversion (Fig. 21(b)), there are two high VP layers. The uppermost one is approximately at the depth interval of 4–6 m and agrees with well data (well A in Fig. 16(b)), where the sand layer extends from 4–6.5 m, followed by peat, where the VP values decrease significantly. Even though the well data are not available for depths

more than 7 m, the high VP layer at a depth deeper than 10 m probably represents the sand since the velocity is close to the shallower high VP layer. The two sand layers are retrieved clearer in the obtained VP model from joint inversion (Fig. 21(b)) than individual BWT (Fig. 21(a)). Figure 22 depicts the corresponding computed ray paths for the VP models in Fig. 21.

Figure 22 shows that the shallower sand layer has been better retrieved by the joint inversion (Fig. 22(b)) than individual BWT inversion, particularly at positions between 45 m and 63 m. The computed Poisson ratio models are shown in Fig. 23, and individual inversion leads to unrealistic values, particularly at the shallow depth where the formation is highly heterogeneous (Fig. 23(a)). The joint inversion algorithm, on the other hand, produced a physically meaningful distribution of the Poisson ratio (Fig. 23(b)) in the whole medium.

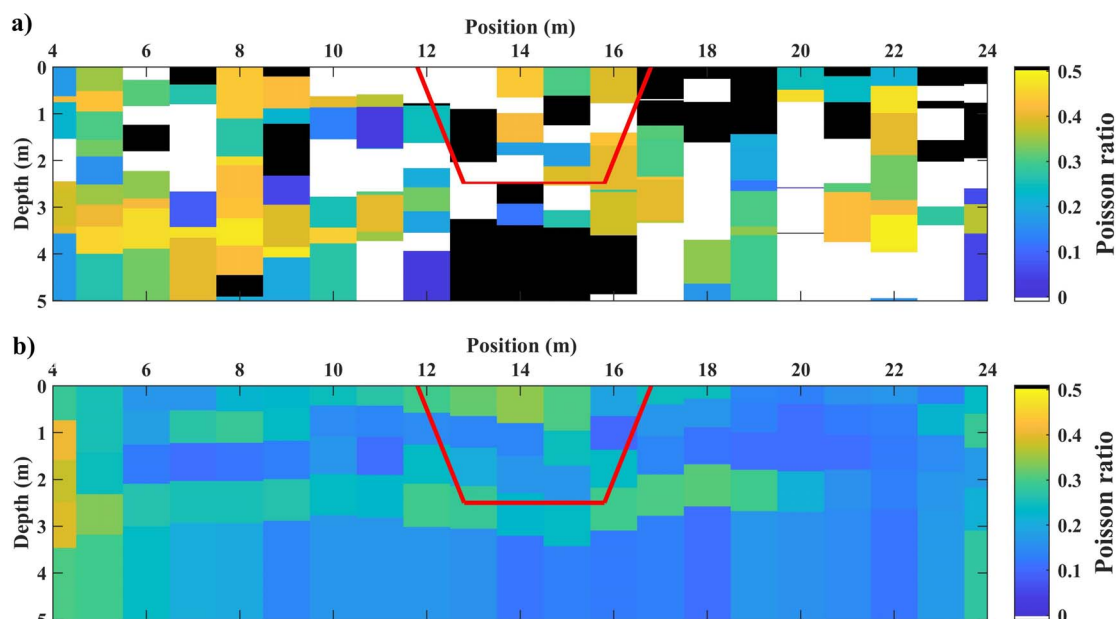


Figure 15 The computed Poisson ratio distribution from (a) individual BWT and SWT inversions and (b) BWT and SWT joint inversion. The shape of the sand deposit is depicted in red lines. The blocks in black or white have non-physical Poisson ratio values.

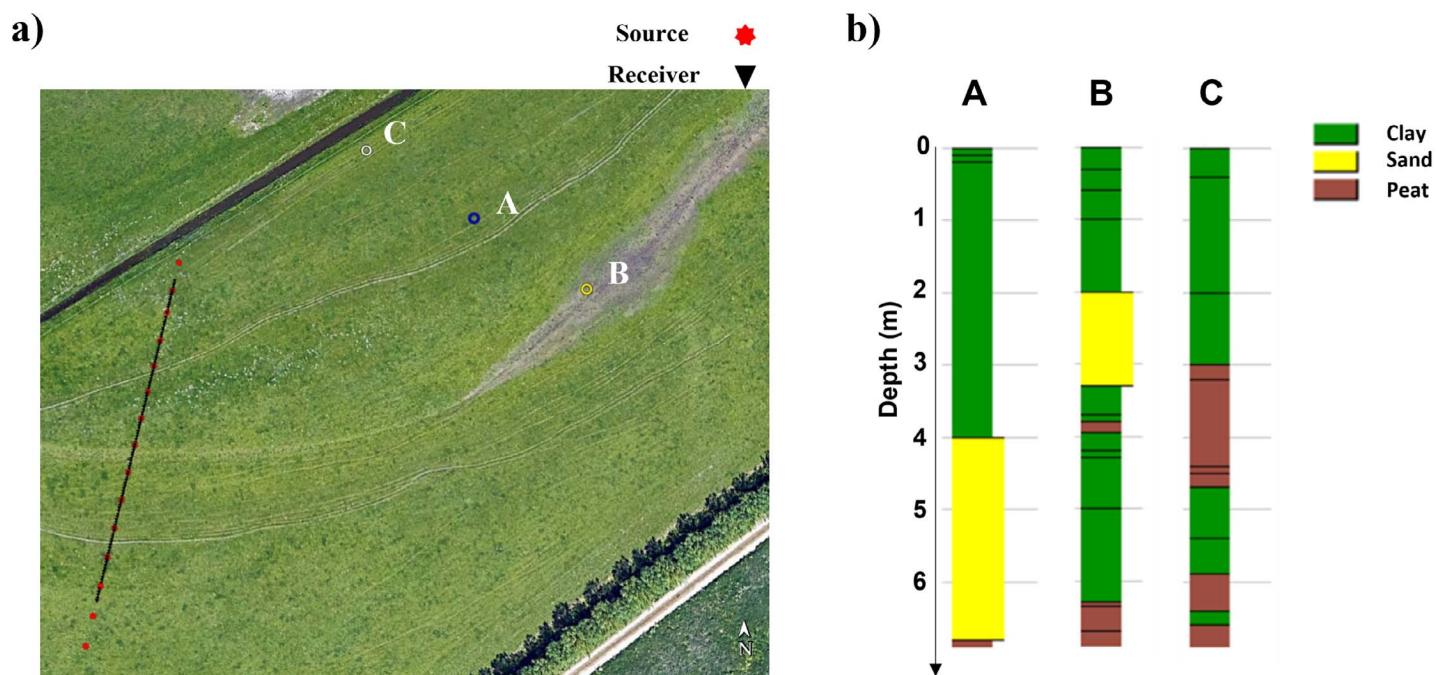


Figure 16 (a) Acquisition scheme and locations of available wells, (b) examples of available well data near to the field.

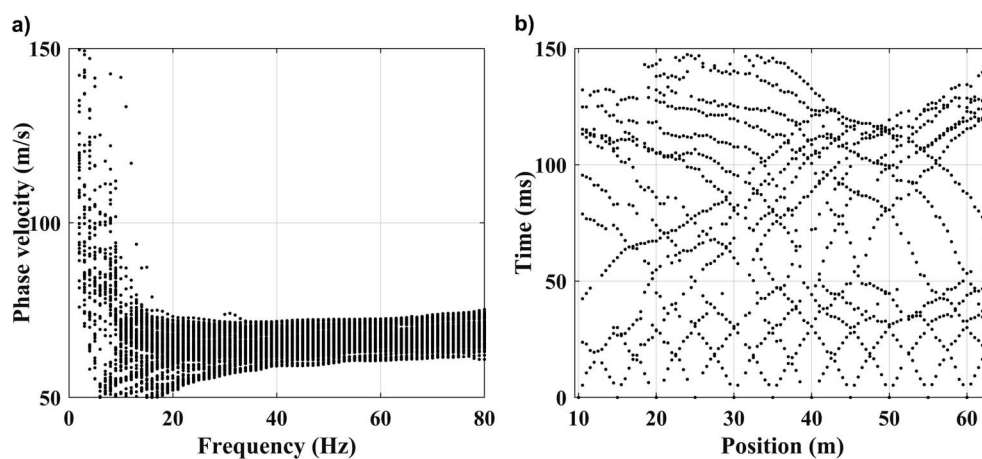


Figure 17 Input data for the inversion. (a) estimated DCs, (b) first arrival times.

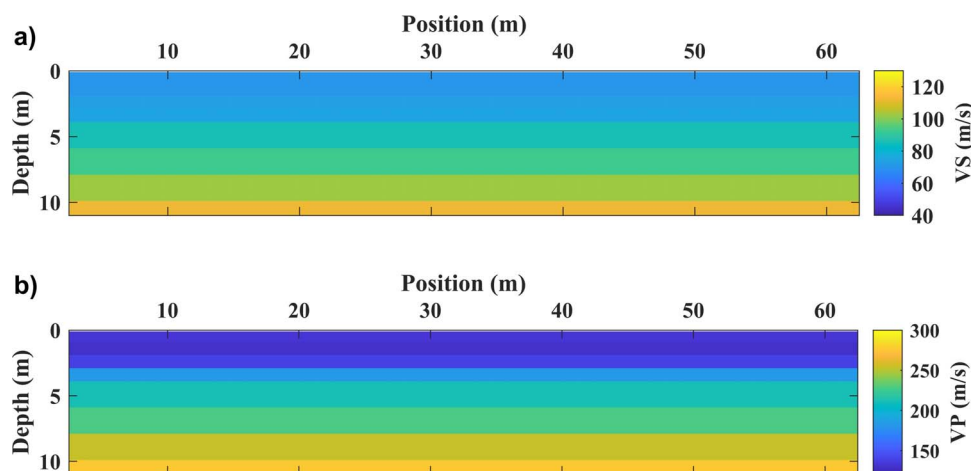


Figure 18 Initial velocity models for the inversion. (a) VS model, (b) VP model.

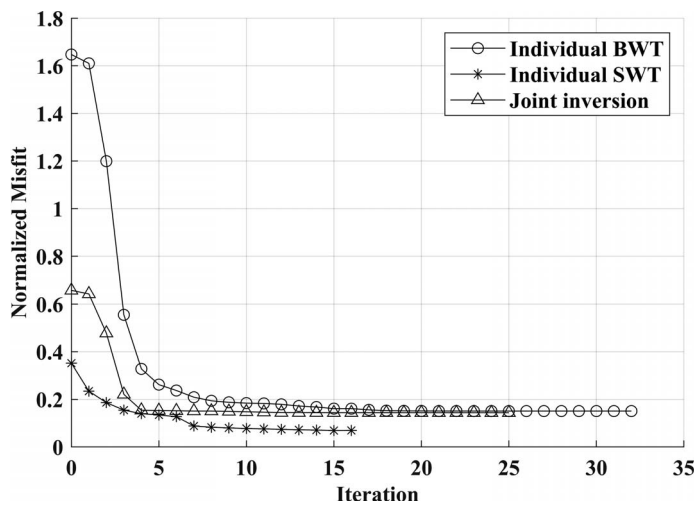


Figure 19 Normalized misfit value as a function of iteration for different inversions.

CONCLUSIONS

We have proposed a joint inversion algorithm to invert dispersion curves and P-wave travel times data to obtain 2D velocity and Poisson ratio models. We have shown that the constructed P-wave and S-wave velocity models by joint inversion of BWT and SWT appear more realistic than individual inversions. From applying the proposed algorithm to synthetic and field datasets, we conclude that the proposed joint inversion scheme produces better subsurface velocity models in terms of recovering layer interfaces and velocity values. The proposed joint inversion algorithm builds physically more meaningful Poisson ratio models, which can retrieve the Poisson ratio distribution accurately. As a future work, we recommend applying the proposed joint inversion algorithm to 3D datasets and investigating the impact of employing

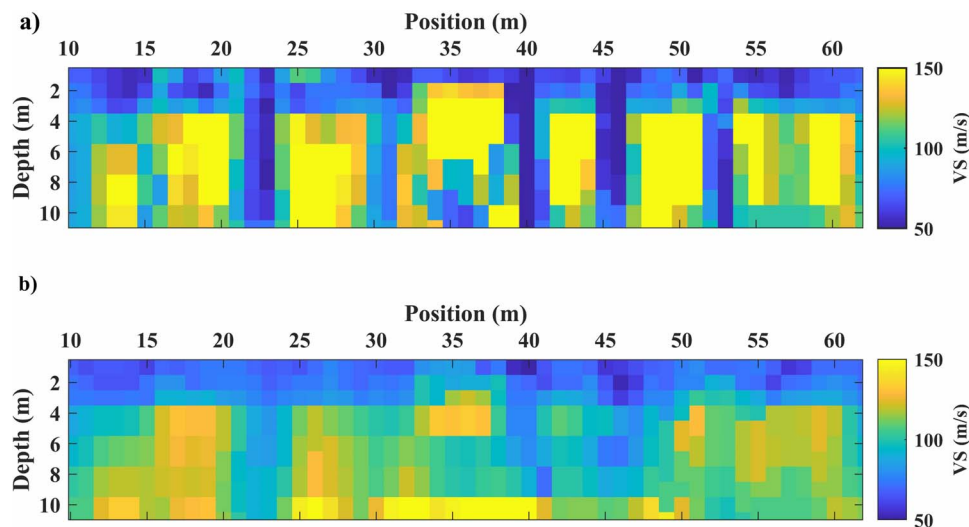


Figure 20 The obtained VS models from (a) individual SWT inversion and (b) BWT and SWT joint inversion. spatial regularization methods.

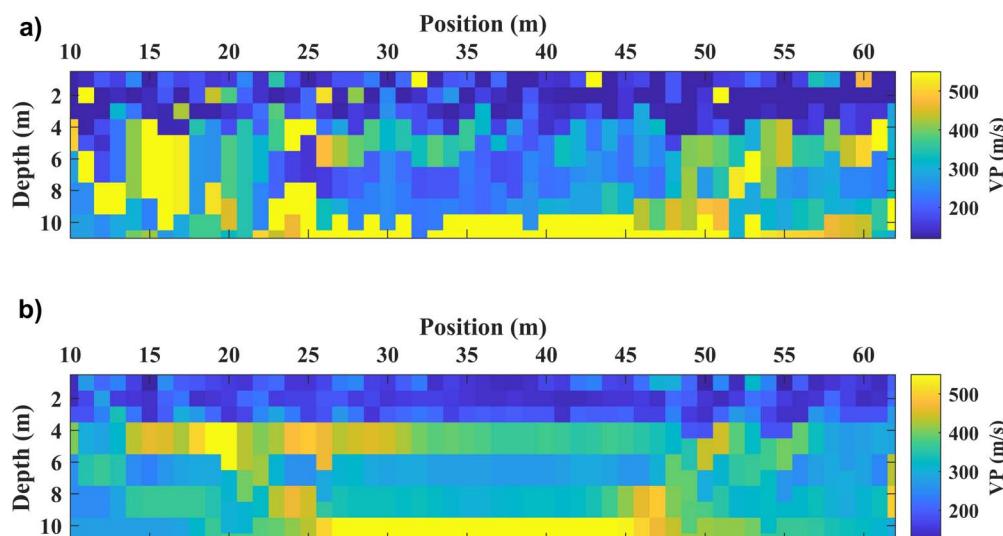


Figure 21 VP models from (a) individual BWT inversion and (b) BWT and SWT joint inversion.

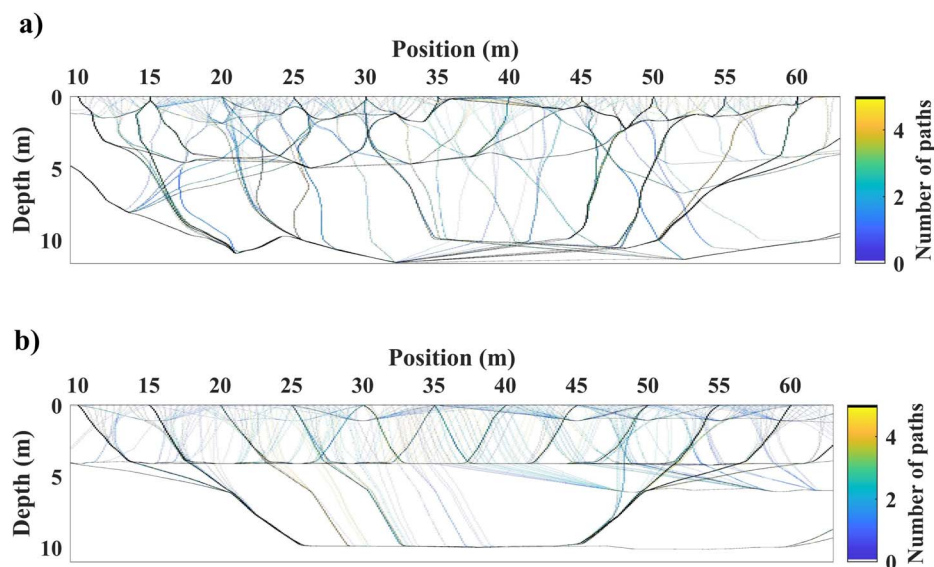


Figure 22 Ray paths of first arrival times from (a) individual BWT and (b) BWT and SWT joint inversion.

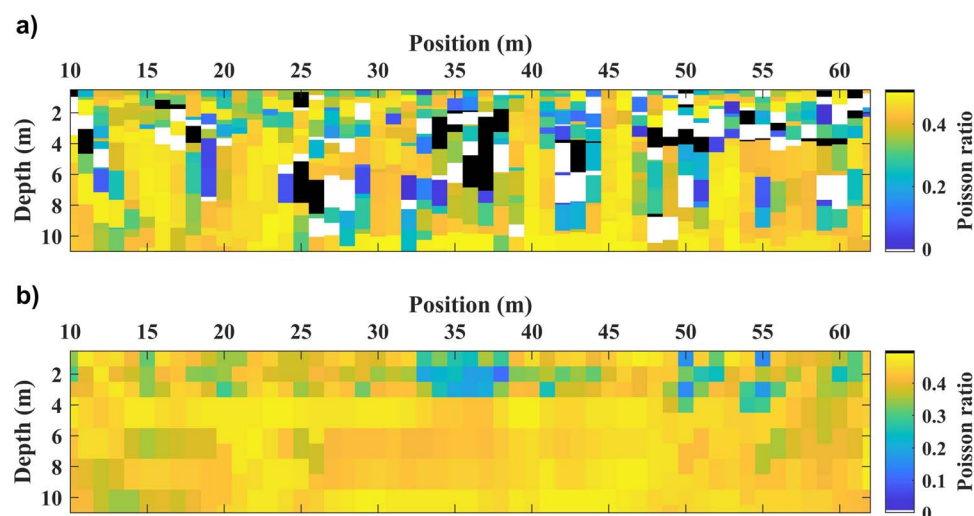


Figure 23 Poisson ratio distribution from (a) individual inversions and (b) BWT and SWT joint inversion. The blocks in white or black have non-physical Poisson ratio values.

References

- Auken, E., and Christiansen, A.V., 2004, Layered and laterally constrained 2D inversion of resistivity data: *Geophysics*, **69**(3), 752–761.
- Bai, P., Vignoli, G., and Hansen, T.M., 2021, 1D Stochastic inversion of airborne time-domain electromagnetic data with realistic prior and accounting for the forward modeling error: *Remote Sensing*, **13**, 3881.
- Bharadwaj, P., Mulder, W.A., Drijkoningen, G.G., and Reijnen, R., 2015, Looking ahead of a tunnel boring machine with 2-D SH full waveform inversion: *in* Expanded Abstracts: 77th EAGE Conference & Exhibition, 1–5.
- Boiero, D., and Socco, L.V., 2010, Retrieving lateral variations from surface wave dispersion curves: *Geophysical Prospecting*, **58**, 977–996.
- Boiero, D., and Socco, L.V., 2014, Joint inversion of Rayleigh-wave dispersion and P-wave refraction data for laterally varying models: *Geophysics*, **79**(4), 49–59.
- Carter-McAuslan, A., Lelièvre, P.G., and Farquharson, C.G., 2015, A study of fuzzy c-means coupling for joint inversion using seismic tomography and gravity data test scenarios: *Geophysics*, **80**(1), 1–15.
- Comina, C., Foti, S., Sambuelli, L., Socco, L.V., and Strobbia, C., 2002, Joint inversion of VES and surface wave data: *Symposium on the Application of Geophysics to Engineering and Environmental Problems*.
- Da Col, F., Papadopoulou, M., Koivisto, E., Sito, L., Savolainen, M., and Socco, L.V., 2020, Application of surface-wave tomography to mineral exploration: a case study from Siilinjärvi, Finland: *Geophysical Prospecting*, **68**(1), 254–269.
- Dell'Aversana, P., Bernasconi, G., Miotti, F., and Rovetta, D., 2011, Joint inversion of rock properties from sonic, resistivity and density well-log measurements: *Geophysical Prospecting*, **59**(6), 1144–1154.
- Gallardo, L.A., and Meju, M.A., 2003, Characterization of heterogeneous near-surface materials by joint 2D inversion of DC resistivity and seismic data: *Geophysical Research Letters*, **30**(13).
- Gao, G., Abubakar, A., and Habashy, T.M., 2010, Simultaneous joint petrophysical inversion of electromagnetic and seismic measurements: *in* Expanded Abstracts: 80th Annual International Meeting, Society of Exploration Geophysics, 2799–2804.
- Garofalo, F., 2014, Physically constrained joint inversion of seismic and electrical data for near-surface application: Ph.D. thesis, Politecnico di Torino.
- Garofalo, F., Sauvin, G., Socco, L.V., and Lecomte, I., 2015, Joint inversion of seismic and electric data applied to 2D media: *Geophysics*, **80**(4), 93–104.
- Ghose, R., and Slob, E.C., 2006, Quantitative integration of seismic and GPR reflections to derive unique estimates for water saturation and porosity in subsoil: *Geophysical Research Letters*, **33**, L05404.

- Haber, E., and Holtzman Gazit, M., 2013, Model fusion and joint inversion: Surveys in Geophysics, **34**, 675–695.
- Hu, W., Abubakar, A., and Habashy, T.M., 2009, Joint electromagnetic and seismic inversion using structural constraint: Geophysics, **74**(6), 99–109.
- Karimpour, M., Slob, E., and Socco, L.V., 2021, Joint inversion of surface wave tomography and body wave tomography applied to 2D media: *in* Expanded Abstracts: 82nd EAGE Annual Conference & Exhibition, 1–5.
- Khosro Anjom, F., 2021, S-wave and P-wave velocity model estimation from surface waves: Ph.D. thesis, Politecnico di Torino, Torino.
- Krohn, C. E., and P. S. Routh, 2017, Exploiting surface consistency for surface-wave characterization and mitigation — Part 1: Theory and 2D examples: Geophysics, **82**, V21–V37.
- Lien, M., 2013, Simultaneous joint inversion of amplitude-versus-offset and controlled-source electromagnetic data by implicit representation of common parameter structure: Geophysics, **78**(4), 15–27.
- Marquardt, D.W., 1963, An algorithm for least squares estimation of nonlinear parameters: Journal of the Society of Industrial Applied Mathematics, **11**(2), 431–441.
- Menke, W., 1989, Geophysical data analysis: discrete inverse theory: Academic Press, San Diego, 152–159.
- Moorkamp, M., Heincke, B., Jegen, M., Roberts, A.W., and Hobbs, R.W., 2011, A framework for 3-D joint inversion of MT, gravity and seismic refraction data: Geophysical Journal International, **184**(1), 477–493.
- Noble, M., Gesret, A., and Belayouni, N., 2014, Accurate 3-D finite difference computation of traveltimes in strongly heterogeneous media: Geophysical Journal International, **199**(3), 1572–1585.
- Ogunbo, J.N., Marquis, G., Zhang, J., and Wang, W., 2018, Joint inversion of seismic traveltime and frequency-domain airborne electromagnetic data for hydrocarbon exploration: Geophysics, **83**, 9–22.
- Papadopoulou, M., 2021, Surface wave methods for mineral exploration: Ph.D. thesis, Politecnico di Torino.
- Papadopoulou, M., Da Col, F., Mi, B., Backstrom, E., Marsden, P., Brodic, B., Malehmir, A., and Socco, L.V., 2020, Surface-wave analysis for static corrections in mineral exploration: A case study from central Sweden: Geophysical Prospecting, **68**(1), 214–231.
- Passeri, F., 2019, Development of an advanced geostatistical model for shear wave velocity profiles to manage uncertainties and variabilities in ground response analyses: Ph.D. thesis, Politecnico di Torino.
- Paulatto, M., Moorkamp, M., Hautmann, S., Hooft, E., Morgan, J.V., and Sparks, R.S.J., 2019, Vertically extensive magma reservoir revealed from joint inversion and quantitative interpretation of seismic and gravity data, Journal of Geophysical Research: Solid Earth, **124**, 11170–11191.
- Piatti, C., Socco, L.V., Boiero, D., and Foti, S., 2013, Constrained 1D joint inversion of seismic surface waves and P-refraction travel times: Geophysical Prospecting, **61**(1), 77–93.
- Qin, T., Zhao, Y., Hu, S., An, C., Bi, W., Ge, S., Capineri, L., and Bohlen, T., 2020, An interactive integrated interpretation of GPR and Rayleigh Wave Data Based on the Genetic Algorithm: Surveys in Geophysics, **41**, 549–574.
- Reynolds, J. M., 1997, An introduction to applied and environmental geophysics: John Wiley & Sons, Chichester, 303–305.
- Tarantola, A., 1987, Inverse problem theory: Methods for data fitting and model parameter estimation: Elsevier Science.
- Teodor, D., Comina, C., Socco, L.V., Brossier, R., Trinh, P.T., and Virieux, J., 2017, Initial model design for full-waveform inversion—preliminary elastic modeling from surface waves data analysis: *in* Extended Abstract in 36th GNGTS national convention, 733–756.
- Vignoli, G., Guillemoteau, J., Barreto, J., and Rossi, M., 2021, Reconstruction, with tunable sparsity levels, of shear wave velocity profiles from surface wave data: Geophysical Journal International, **225**(3), 1935–1951.
- Wagner, F.M., Mollaret, C., Günther, T., Kemna, A., and Hauck, C., 2019, Quantitative imaging of water, ice and air in permafrost systems through petrophysical joint inversion of seismic refraction and electrical resistivity data: Geophysical Journal International, **219**, 1866–1875.

Acknowledgments

The Ph.D. scholarship of Mohammadkarim Karimpour is funded by Compagnia di San Paolo in the framework of the Joint Project Program. We also thank the CNR group for giving access to data acquisition and Seismic Mechatronics for providing the vibrator source.